catalysts

MDPI

Article

Comparative Photo-Electrochemical and Photocatalytic Studies with Nanosized TiO_2 Photocatalysts towards Organic Pollutants Oxidation

Damián Monllor-Satoca [1], Pedro Bonete [1,*], Ridha Djellabi [2,3], Giuseppina Cerrato [4], Lorenza Operti [4], Roberto Gómez [1] and Claudia Letizia Bianchi [2,3,*]

[1] Institut Universitari d'Electroquímica i Departament de Química Física, Universitat d'Alacant, Apartat 99, E-03080 Alacant, Spain; damian.monllor@ua.es (D.M.-S.); roberto.gomez@ua.es (R.G.)
[2] Dipartimento di Chimica, Università degli Studi di Milano, via Golgi 19, 20133 Milano, Italy; ridha.djellabi@yahoo.com
[3] Consorzio Interuniversitario per la Scienza e Tecnologia dei Materiali (INSTM), via Giusti 9, 50121 Firenze, Italy
[4] Dipartimento di Chimica & NIS Centre of Excellence, Università degli Studi di Torino, via Giuria 7, 10125 Torino, Italy; giuseppina.cerrato@unito.it (G.C.); lorenza.operti@unito.it (L.O.)
* Correspondence: pedro.bonete@ua.es (P.B.); claudia.bianchi@unimi.it (C.L.B.); Tel.: +39-0250314253 (C.L.B.)

Abstract: The size of TiO_2 can significantly affect both its photocatalytic and photo-electrochemical properties, thus altering the photooxidation of organic pollutants in air or water. In this work, we give an account of the photo-electrochemical and photocatalytic features of some nanosized TiO_2 commercial powders towards a model reaction, the photooxidation of acetone. Cyclic voltammograms (CV) of TiO_2 particulate electrodes under UV illumination experiments were carried out in either saturated O_2 or N_2 solutions for a direct correlation with the photocatalytic process. In addition, the effect of different reaction conditions on the photocatalytic efficiency under UV light in both aqueous and gaseous phases was also investigated. CV curves with the addition of acetone under UV light showed a negative shift of the photocurrent onset, confirming the efficient transfer of photoproduced reactive oxygen species (ROSs), e.g., hydroxyl radicals or holes to acetone molecules. The photocatalytic experiments showed that the two nano-sized samples exhibit the best photocatalytic performance. The different photoactivity of the larger-sized samples is probably attributed to their morphological differences, affecting both the amount and distribution of free ROSs involved in the photooxidation reaction. Finally, a direct correlation between the photocatalytic measurements in gas phase and the photo-electrochemical measurements in aqueous phase is given, thus evincing the important role of the substrate-surface interaction with similar acetone concentrations.

Keywords: nanosized TiO_2; photocatalytic efficiency; photo-electrochemical characterization; environmental remediation

Citation: Monllor-Satoca, D.; Bonete, P.; Djellabi, R.; Cerrato, G.; Operti, L.; Gómez, R.; Bianchi, C.L. Comparative Photo-Electrochemical and Photocatalytic Studies with Nanosized TiO_2 Photocatalysts towards Organic Pollutants Oxidation. *Catalysts* **2021**, *11*, 349. https://doi.org/10.3390/catal11030349

Academic Editor: Ioannis Konstantinou

Received: 17 February 2021
Accepted: 2 March 2021
Published: 9 March 2021

1. Introduction

Semiconductor photocatalysts have been intensively investigated because of their applicability in the treatment of pollutants in both air and water phases. Titanium dioxide (TiO_2), a wide band gap semiconductor (3.0–3.2 eV), exhibits an excellent reactivity that enables it to photo-abate organic pollutants, ubiquitous in the environment from both natural and anthropogenic origin [1–3]. Moreover, the last decade has witnessed a rapid growth on the nanotechnology field, leading to the increasing use of TiO_2 nanopowders in industrial and commercial products [4,5]. The extremely small size of nanopowder crystallites confers them a high specific surface area, which may result in a prospectively greater reactivity compared to larger sized powders [6].

Up to now, widespread attention has been directed to the development of TiO_2 powders with very small crystallite size in an effort to enhance the photocatalytic activity and

process efficiency. However, great concerns have risen in the last years on the effective toxicity of nanoparticles. Particles with diameters below 100 nm fall into the classification of "ultrafine" materials (nanoparticles) [7], and some studies reported that these particles are linked with several adverse health effects [8,9]. Ultrafine particles may be highly harmful for humans because of their capability to deeply penetrate lungs and cell membranes [10] causing lung tumors, inflammations, fibrosis, DNA damage [11] and cytotoxicity [12,13]. In order to substitute nano-sized particles in industrial and environmental remediation processes, the current research is investigating the photocatalytic efficiency of TiO_2 materials possessing larger crystallite size. In particular, some reports have successfully demonstrated the interesting catalytic performance of commercial sub-micro-sized TiO_2 powders sold as pigmentary materials [14,15]. The efficiency has been tested towards the photodegradation of (i) both NO_x and volatile organic compounds (VOCs) in gas phase and (ii) some organic dyes dissolved in water [16,17].

Parallel to this, nanostructured TiO_2 electrodes have also been extensively studied as photoanodes for photo-electrochemical water splitting [18–21] and water remediation [22–26]. One peculiar feature of the electrochemical measurements is that the oxidation and reduction reactions can be carried out separately and studied independently. In this way, it becomes possible to gain information on the limiting reaction rate of the individual processes, leading to a clear account of the changes and modifications that could occur on the TiO_2 surface. In several reports, the photo-electrochemical properties of TiO_2 nanoelectrodes were investigated with the aim to study their electronic structure and photoefficiency through electrochemical measurements [27–29]. In particular, the research on the electrochemical properties of TiO_2 electrodes pointed out that the photoefficiency depends on the particle morphology, including size and shape [30–33]. In fact, nanoparticle shape and preferential surface orientation of its facets play an important role in the electrochemical oxidation because these factors affect not only the reactants but also the interfacial charge transfer. In comparison with their larger counterparts, it is likely that the nano-sized powders suffer from an increased charge recombination rate at the surface, due to the large density of surface states that could act as carrier trapping sites; on the contrary, the larger-sized powders could sustain a built-in electric potential within the particles, which is able to generate a space charge region that facilitates charge separation, thus preventing surface recombination. Consequently, hindering the recombination of photogenerated charge carriers is essential for improving the efficiency of net charge transfer at the semiconductor/electrolyte interface (SEI). In this respect, many factors can influence the overall electrochemical response, including electrode thickness, surface area and particle size. The correct control of these parameters is thus essential.

The purpose of this paper is to compare the properties of four nanosized TiO_2 commercial powders through photo-electrochemical and photocatalytic measurements of the degradation of acetone. In particular, we chose to investigate the oxidation of acetone on TiO_2 as a model reaction to probe its photocatalytic activity. In order to get a correct comparison between electrochemical and photo-electrochemical experiments, the electrochemical analysis was conducted in both saturated N_2 and O_2 solutions. This way, it is possible to independently monitor the reduction and oxidation processes. In addition, to gain further mechanistic information, photo-electrochemical analyses were also conducted for different acetone solution concentrations, investigating the influence of the amount of pollutant on the photoefficiency.

2. Results and Discussion

2.1. Characterization of the Titania Powders

The surface area of nano-sized powders, analyzed by means of the BET method, is higher than that of the larger-sized samples, as expected [14]. P25 and PC105 show a surface area of 50 and 80 m^2/g, respectively, while 1077 and AH-R show much lower values (~12 m^2/g). The XRD spectra reveal the presence of the pure anatase phase for all the quoted samples but P25, which contains a 75:25 ratio of anatase-to-rutile phase [34]. The

morphological aspects of all samples were examined by HR-TEM (Figure 1). Nanometric powders (P25 and PC105) exhibit the typical average particle size of 20–30 nm. Furthermore, the nanosized materials are homogeneous with well-packed crystalline particles. In parallel with this, a distinctive morphology could be noticed in the larger-sized samples (1077 and AH-R). The average crystallite size of the anatase, calculated via Scherrer's formula, falls into the 100–130 nm range. In all cases, the analyses of the fringe patterns (either as such or by means of the FFT elaboration) reveal the presence of the (101) family of planes ascribable to the anatase phase (ICDD card n. 21-1272).

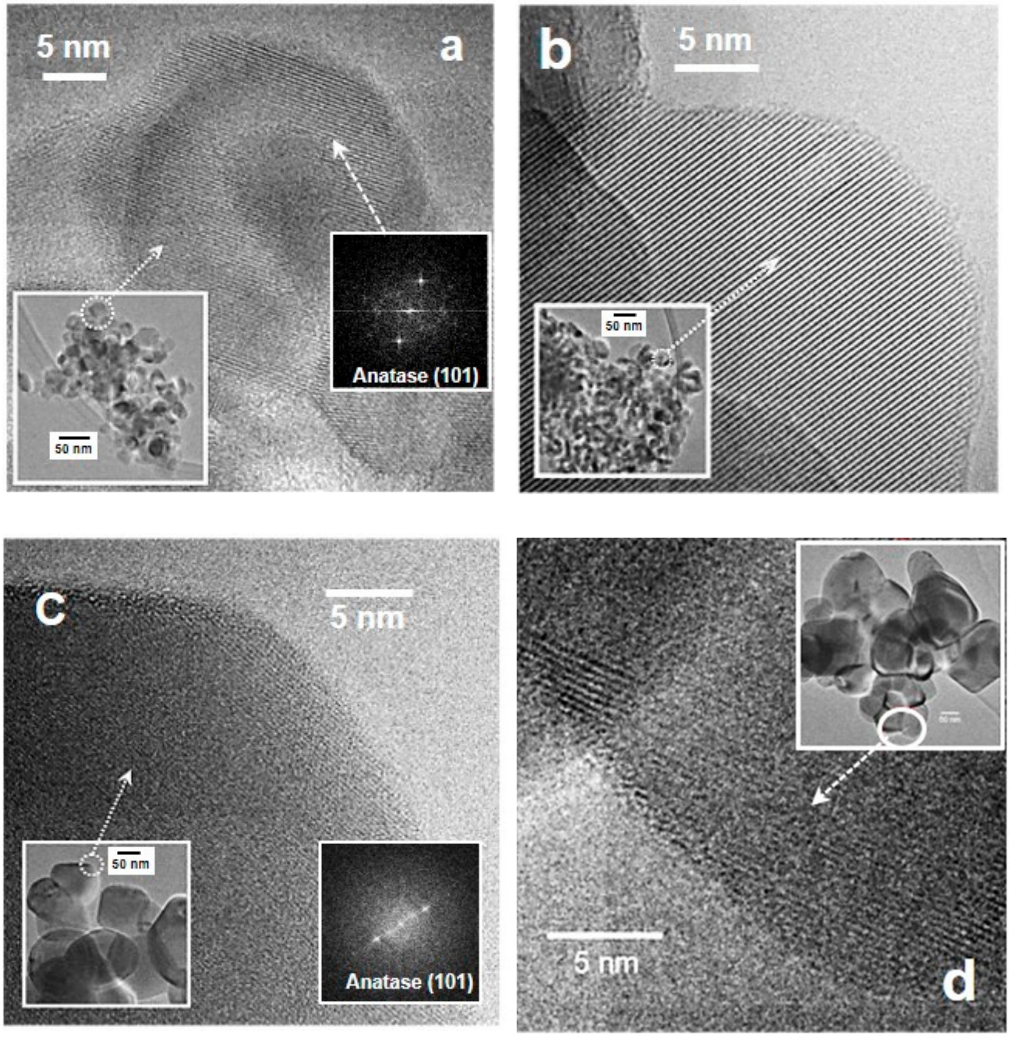

Figure 1. HR-TEM images of P25 (**a**) and PC105 (**b**) nanosized samples; 1077 (**c**) and AH-R (**d**) sub-microsized samples. Insets in all panels show a 50 nm scale image of the samples. Panels (**a**) and (**c**) also show electron diffraction patterns.

Finally, the average thickness of the respective films (as measured by profilometry in two different sections of the TiO_2 annealed film) was about 3 μm for both nanometric and sub-micrometric samples.

It is well known that surface hydroxyls are crucial species for the photocatalytic process. In particular, photo-generated holes may react with water molecules adsorbed on semiconductor surfaces, resulting in the formation of trapped holes as OH radicals [14]. To show the prospective formation of these radicals, FTIR spectra of the samples in the ν(OH) spectral range in air (black lines) and after outgassing at RT (red lines) are reported in Figure 2. All the materials in air exhibit two complex absorption bands, respectively located in the 3000–3450 cm^{-1} range and at $\nu \geq 3600$ cm^{-1}. On the basis of the spectral behavior

and of the literature data [35,36], the former broad peak can be ascribed to the stretching mode of all H–bonded OH groups present at the surface of the various solids, whereas the latter corresponds to the stretching mode of all the Ti–OH species free from hydrogen bonding interactions. Comparing the spectra of smaller-sized samples with that of larger-sized TiO_2, it is evident that nano-sized samples are characterized by a significantly higher amount of hydroxyl species. In particular, PC105 shows the highest amount of OH groups among the samples studied, where the absorbance of PC105 has been halved. Moreover, nano-sized surface samples are characterized by an uneven distribution of terminal Ti–OH species in comparison with their micro-sized counterparts (1077 and AH-R).

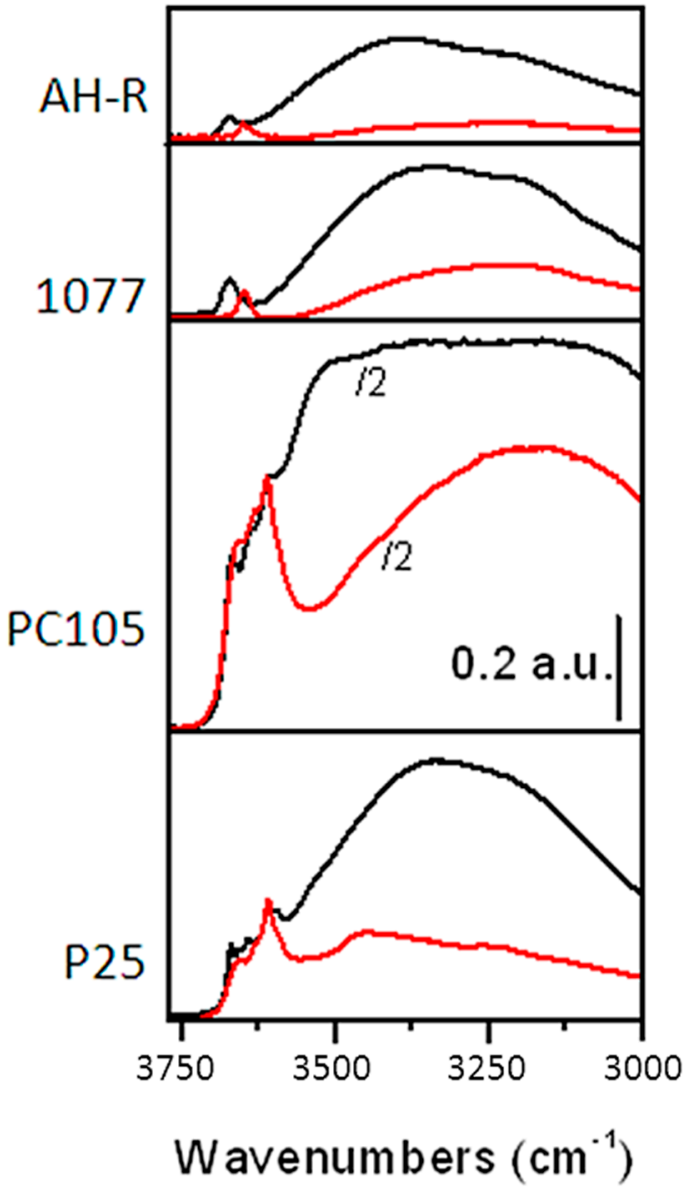

Figure 2. Absorbance IR spectra in the OH stretching region for the different samples (P25, PC105, 1077, AH-R) in air (black lines) and after outgassing at RT for 60 min (red lines). The absorbance depicted for PC105 sample has been divided by 2.

After outgassing at RT (Figure 2, red lines) physisorbed water molecules are removed and, as a consequence, the absorbance of the envelope related to H–bonded OH groups decreases significantly. For the larger-sized TiO_2, the band related to Ti–OH shifts toward lower frequency upon outgassing, indicating that physisorbed water alters the reactivity of

Ti–OH groups. In particular, a band at lower frequency points to the presence of hydroxyl groups with a more acidic character.

2.2. Photo-Electrochemical Analysis

In photo(electro)catalysis, two separate processes take place simultaneously: the oxidation process based on photogenerated hole transfer and the reduction process with photogenerated electrons, which can be separately studied, including their kinetics, by electrochemical methods. Moreover, it is of great interest to correlate the photo-electrochemical and photocatalytic behavior of the smaller TiO_2 samples (P25 and PC105), in comparison with that of larger ones (AH-R and 1077).

Regarding the oxygen reduction process, Berger et al. experimentally established that the accumulation region onset reflects the conduction band and surface state properties and that the associated current is correlated to the active surface area [37,38]. Figure 3 shows the voltammograms in the dark for TiO_2 samples in a 0.1 M $HClO_4$ aqueous solution in the presence and the absence of oxygen. In the absence of oxygen, the voltammetric response is dominated by the accumulation region appearing at potentials below −0.2 V vs. Ag/AgCl. As expected, the capacitance of the nanocrystalline electrodes is much larger than that of the sub-microcrystalline ones, as the interfacial area of the nanocrystalline electrodes is expected to be much larger for the same electrode thickness. The shown reductive currents are directly associated to the accumulation of electrons in the TiO_2 film. Nanometric samples (P25 and PC105) show higher reduction currents in agreement with the literature, [39] which is likely related to the higher internal surface area of these samples with respect to sub-microsized ones. In any case, the onset of the oxygen reduction current is similar in all cases and coincides with the onset of the accumulation region.

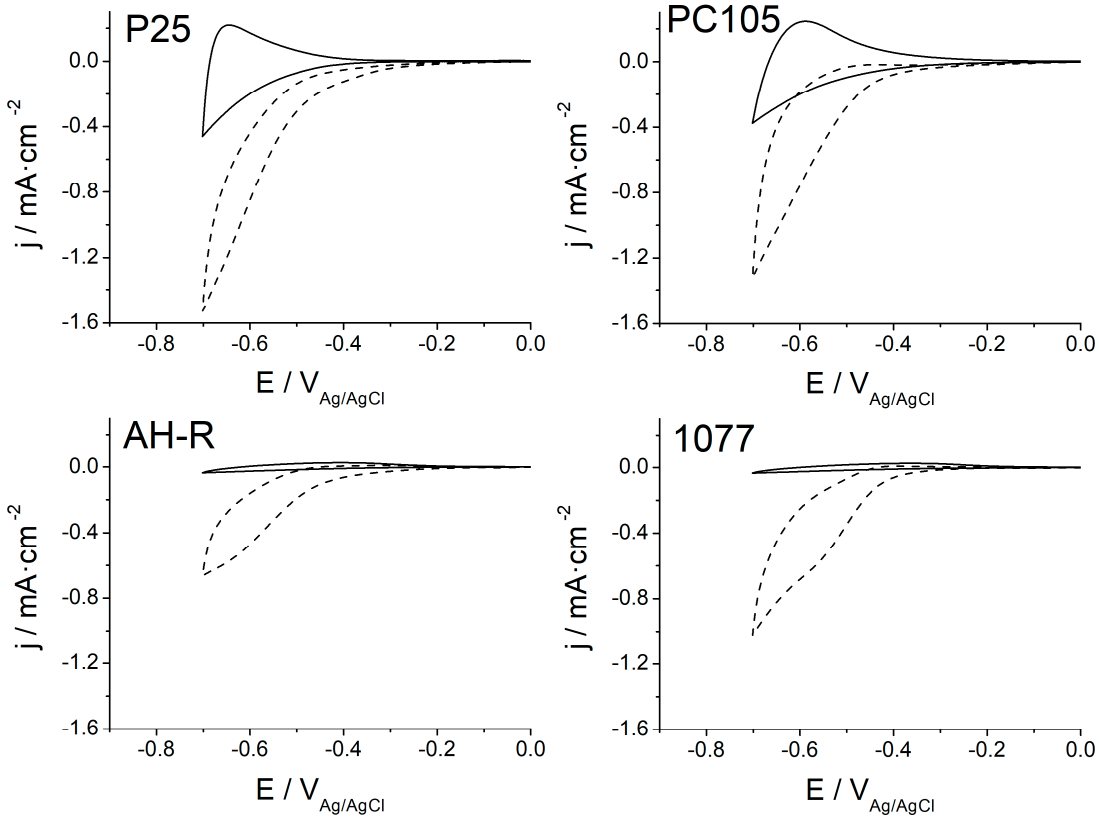

Figure 3. Voltammograms in the dark for nano-sized (P25 and PC105) and sub-micro-sized (1077 and AH-R) electrodes in 0.1 M HClO4 solution in the presence (—) and in the absence (—) of oxygen.

Prior to presenting and discussing the photo-electrochemical results, it is interesting to obtain information on the double layer structure in each of these types of electrodes. In the case of nanocrystalline electrodes, the existence of significant band bending within the particles is discarded, as their mesoporous nature and small particle diameter precludes the formation of a sizable in-built electric potential gradient. However, this is not necessary the case of microcrystalline electrodes.

For testing this in the case of a larger-sized TiO_2 electrode, the potential dependence of capacitance was analyzed using the Mott–Schottky (M–S) theory in the case of the AH-R sample. A linear behavior in the ${C_{sc}}^{-2}$ vs. E plot would point to the existence of a space charge layer within each particle. In addition, both the donor concentration, N_D, and the flatband potential, E_{fb}, of the semiconductor electrode can be estimated. The M–S equation can be written as:

$$C_{SC}^{-2} = \left(\frac{2}{\varepsilon\varepsilon_0 e N_D}\right)\left(E - E_{fb} - kT/e\right) \quad (1)$$

where C_{sc} represents the differential capacitance of the space charge layer. The flat band potential is given by extrapolation to $C^{-2} = 0$. Figure 4 shows the M–S plot for the TiO_2 electrode AH-R. A good linear correlation is found in a relatively wide potential range. This is interesting as it is compatible with the large particle size of AH-R sample sustaining a space charge layer. The value of E_{fb} results to be around -0.6 V. This behavior is mainly determined for the particle size in the case of particulate electrodes, and it can thus be anticipated for electrodes of this kind.

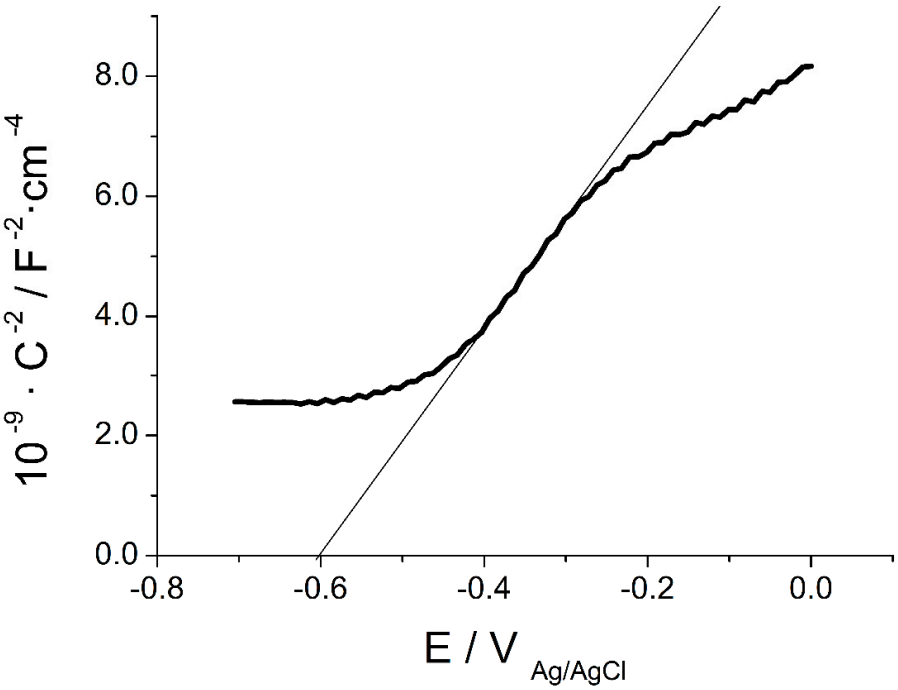

Figure 4. Mott–Schottky plot for the electrode made up of AH-R particles.

The behavior of the different electrodes toward photooxidation processes was investigated. Figure 5 shows voltammograms under UV illumination as a function of the acetone concentration for all the samples under scope. The response in the absence of acetone is attributed to the photooxidation of water, while in its presence, the photooxidation of the organic compound should prevail. The latter can be deduced from the negative shift of the photocurrent onset observed upon the addition of acetone, which indicates that acetone photooxidation is easier than that of water, as acetone scavenges holes more easily than water [40], thus reducing the overpotential for its oxidation.

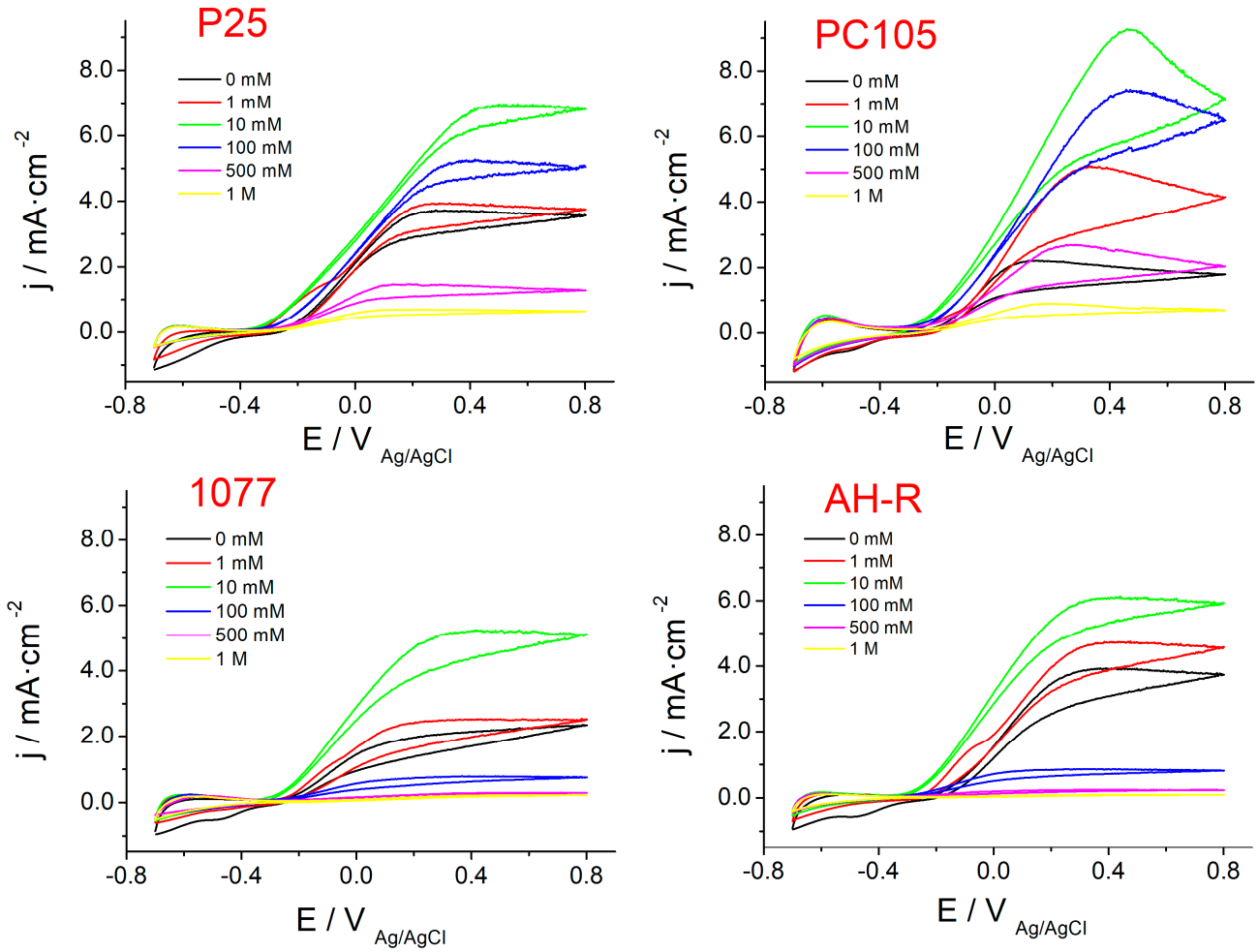

Figure 5. Voltammograms using UV light of smaller-sized (P25 and PC105) and larger-sized samples (AH-Rand 1077) in 0.1 M $HClO_4$ and acetone at different concentrations.

Figure 6 corresponds to the stationary photocurrent density (at 0.6 V) vs. acetone concentration plots for the same electrodes. The oxidation photocurrent increases with the concentration of acetone up to 10 mM and then decreases until a near-negligible photocurrent at 1 M of acetone. The values of the photocurrent under otherwise the same conditions depend on the TiO_2 type, but the characteristic trend is similar for all samples. The maximum current recorded using 10 mM acetone for the nano TiO_2 samples, P25 and PC105, is in the range of 7–9 mA/cm^2, whereas for 1077 and AH-R electrodes the values are slightly lower (5.5–6 mA/cm^2). The adsorption of acetone on the surface of the TiO_2 film might explain the trend observed for the photocurrent as the acetone concentration in the electrolyte is increased. The addition of acetone (<10 mM) increases the photocurrent because either free or trapped holes react easily with the acetone adsorbed on TiO_2 allowing for an enhancement of the oxidative process. However, a further increase of the concentration of acetone gradually decreases the observed photocurrent maybe according to a strong adsorption of the pollutant that diminishes the formation of $OH^{\cdot}$. For acetone concentrations higher than 1 M, very low photocurrents can be recorded probably due to a complete inhibition of the anodic process by blocking the TiO_2 electrode surface.

Therefore, the oxidative activity of the prepared TiO_2 electrodes reaches a maximum at lower acetone concentration values around 10 mM. These observations are in agreement with the inhibition of the formic acid photooxidation on TiO_2 resulting from the addition of relatively small amounts of acetone [41]. It is remarkable that the photocurrent onset is located at slightly more negative potentials in the case of nanosized samples indicating a lower recombination rate. In the case of microcrystalline electrodes (AH-R), the flat band

potential as determined from the Mott–Schottky plot is located at potentials more negative (by more than 0.2 V) than the onset potential, which unveils that substantial recombination occurs even in the presence of the organics.

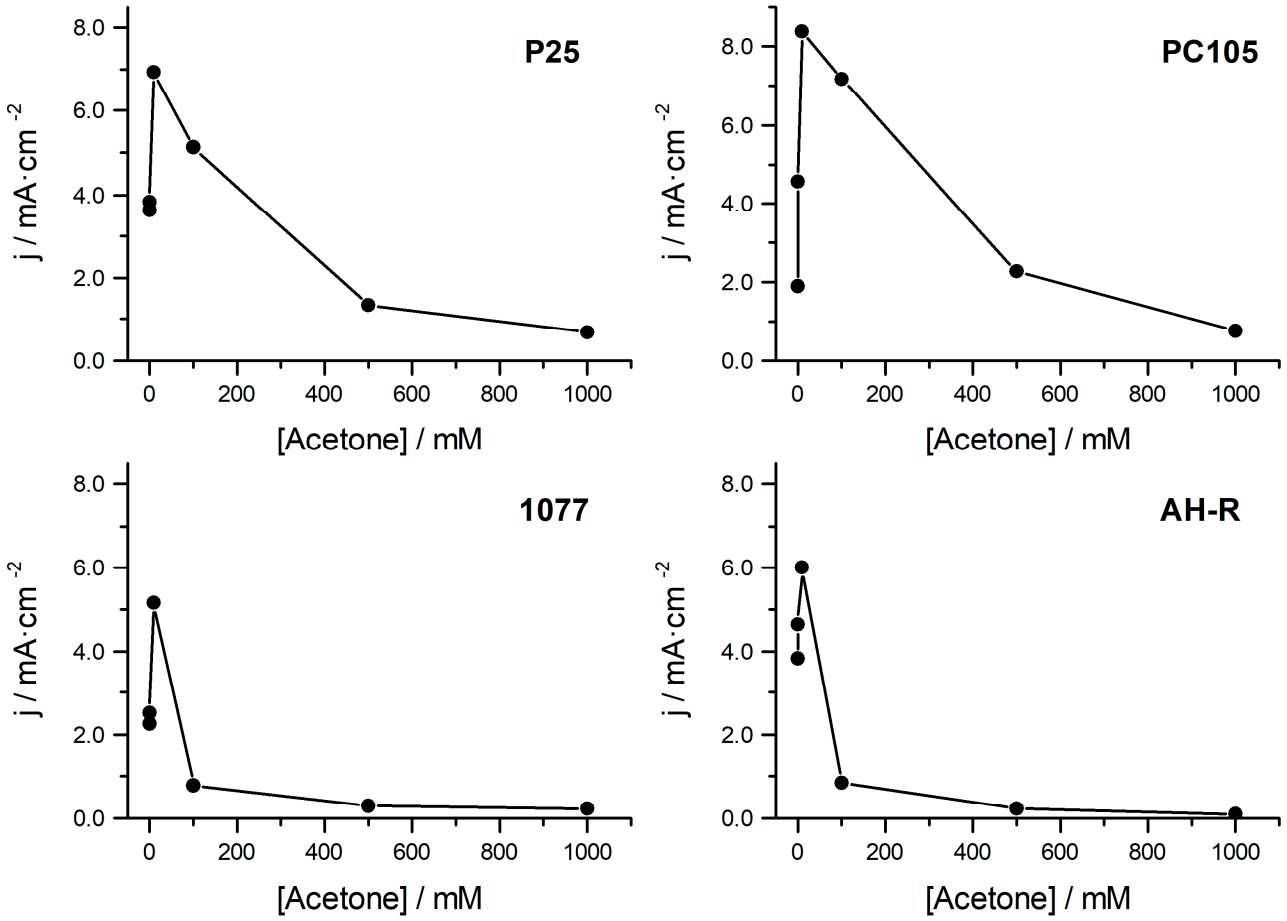

Figure 6. Photocurrent density plots vs. acetone concentration recorded at +0.6 V in 0.1 M $HClO_4$ for smaller-sized (P25 and PC105) and larger-sized electrodes (AH-R and 1077).

To gain more information about the potential activity of these powders as photo-electrocatalysts, in Figure 7, the current density under illumination for the different TiO_2 electrodes corresponding to the photooxidation of acetone (dashed line) together with the current density in the dark corresponding to the reduction of oxygen (solid line) are plotted together. According to the Wagner–Traud principle, the intersection point gives the value of the photocurrent (acetone oxidation) and the dark current (oxygen reduction) under open circuit conditions (i.e., under the typical conditions of suspended photocatalysts). This approach allows us to correlate both photo-electrochemical and photocatalytic measurements, as the latter is a particular case of the former where under open-circuit condition, the rates (or currents) of the anodic and cathodic processes are matched [42]. Figure 7 shows that the P25 powder gives the fastest acetone oxidation of all the samples checked. PC105 and AH-R would have very similar photoactivities, while 1077, would show the lowest photoefficiency. The significant differences found among the different TiO_2 powders highlight that P25, thanks to its peculiar properties, like high surface area, the presence of rutile and the particle morphology, happens to show the best photoefficiency. In particular, we believe that P25 efficiency is highly enhanced by the presence of both phases. The offset between the energetic locations of the conduction band and valence band edges for rutile and anatase should favor charge separation and diminish recombination. In general, there are two opposite factors that should play a key role in determining the photoactivity of powdered TiO_2 samples and electrodes: (i) a high

interfacial area in nanocrystalline samples, which is particularly desirable in the case of substances present at low concentrations; and (ii) the existence of a space charge in microcrystalline samples, diminishing recombination and enhancing photoactivity. Because of the existence of these opposing factors, it is understandable that particular nanocrystalline and microcrystalline samples could exhibit similar photoactivities. Thus, according to our electrochemical measurements, the photoefficiency of the studied TiO_2 samples follows the trend: P25 > PC105 ≈ AH-R > 1077.

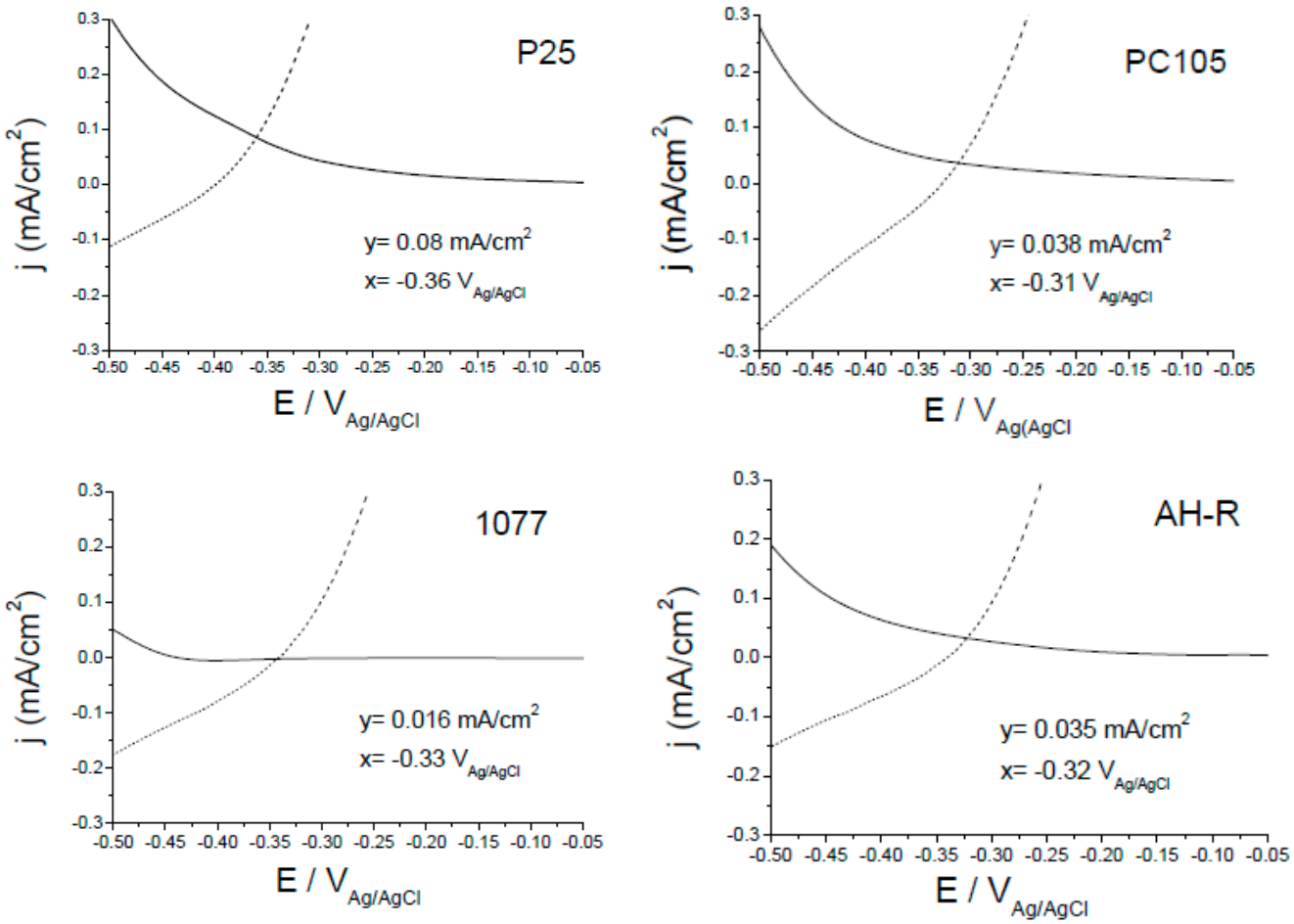

Figure 7. Current density plots for the TiO_2 electrodes on 0.1 M $HClO_4$ + 10 mM acetone solution corresponding to the photooxidation of acetone (——) and the reduction of oxygen (——) in the dark (the latter, as its absolute value).

2.3. Photodegradation Results

Photocatalytic processes are based on the high oxidative potential of photogenerated holes either free or at the catalyst surface. When the TiO_2 is irradiated with UV light, electrons are promoted to the conduction band with the formation of holes on the valence band, leading to charge separation. These highly reactive species can promote oxidation and reduction reactions. The reaction of radical species generated through the capture of holes together with the direct transfer of holes, are the main steps in the photodegradation of many organic compounds, like acetone, adsorbed on the surface of TiO_2.

In Figure 8, the degradation of acetone on the four studied TiO_2 samples is reported. The photoefficiency of AH-R is lower than the activity obtained to P25 and PC105 (nanosized), that is, it follows the sequence P25 ≈ PC105 > 1077 > AH-R with an inversion of the two larger-sized samples behavior as previously observed in the photo-electrochemical measures. Smaller-sized samples show the best photocatalytic performance, leading to a complete degradation of acetone within 1 h. A reason for the different relative photoactivity of AH-R and 1077 could be due to morphological differences, which reflect into a distribu-

tion of free ROSs including hydroxyl radicals, involved in the photooxidation as confirmed by FTIR characterization. It is important to mention that the particle size of the TiO_2 can affect strongly the adsorption of acetone species. Generally, the smaller the particle size of TiO_2 leads to the larger surface area and higher adsorption of acetone species, which in turn facilitates their degradation by photoproduced ROSs on the surface of TiO_2. In addition, in nanosized TiO_2 system, the yield of photoproduced hydroxyl radicals and their diffusion length could be further enhanced compared to sub-micro-sized TiO_2 system.

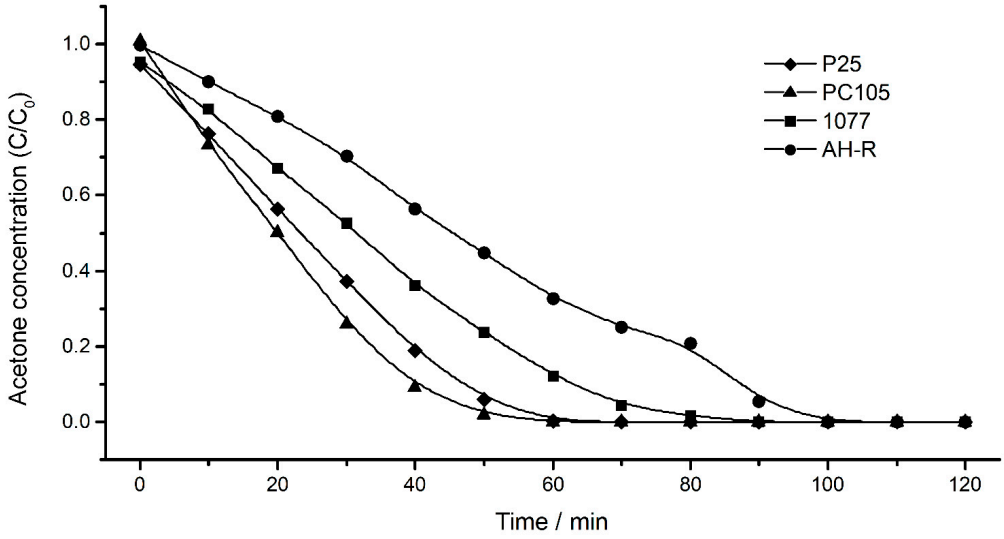

Figure 8. Photocatalytic acetone degradation with smaller-sized (P25 and PC105) and larger-sized (1077 and AH-R) TiO_2 samples. Initial acetone concentration (C_0) is 400 ppmv.

As previous reported by Bianchi et al. [14], the photodegradation of acetone in gas phase is highly influenced by the amount of OH available on the catalytic surface. The presence of high yield of OH groups on the surface of TiO_2 (see the spectra reported in Figure 2) can lead to higher yield of photogenerated reactive oxygen species which in turn enhances the oxidation of acetone. Thus, nanosized samples have the highest photocatalytic activity, because of the high degree of hydroxylation of their surfaces, as shown by the IR spectra. However, larger-sized TiO_2 still exhibits a photodegradation comparable to nanometric samples. To shed light on this issue, Figure 9 reports the XPS spectra for both microcrystalline samples. Peak I is O1s attributed to bulk O while peaks II and III would correspond to bridging and terminal OH groups [43]. The ratio OH/O^{2-} is 0.32 and 0.12, respectively, for 1077 and AH-R. This dissimilarity between the two larger-sized powders confirms the fundamental role of •OH radicals in the photocatalytic process and explains the faster photooxidation with the 1077 sample (see Figure 8).

2.4. Comparison between the Photo-Electrocatalytic Experiments in Aqueous Phase and Photocatalytic Experiments in Gas Phase

Once all information from the measurements has been scrutinized, we shall attempt to semi-quantitatively compare both processes in different reactive media, i.e., photo-electrocatalytic in aqueous phase (PEC) and photocatalytic in gas phase (PC). Presumably, the features of each media might affect the photoactivity of acetone oxidation. In order to evince these differences, we need to use comparable units for the reaction rates in both cases; as reference magnitude, we will use the open-circuit current density for PEC measurements (j_{PEC}) as estimated in Figure 7, whereas we shall calculate an apparent open-circuit current density for PC measurements (j_{PC}) from kinetic data in Figure 8. It is worth mentioning that the analysis is pertinent in terms of the substrate concentration as our experimental conditions are comparable in both phases, provided the acetone concentration is ca. 7 mM in gas phase and 10 mM in aqueous phase. To estimate j_{PC} and compare it with j_{PEC}, we will make the next assumptions:

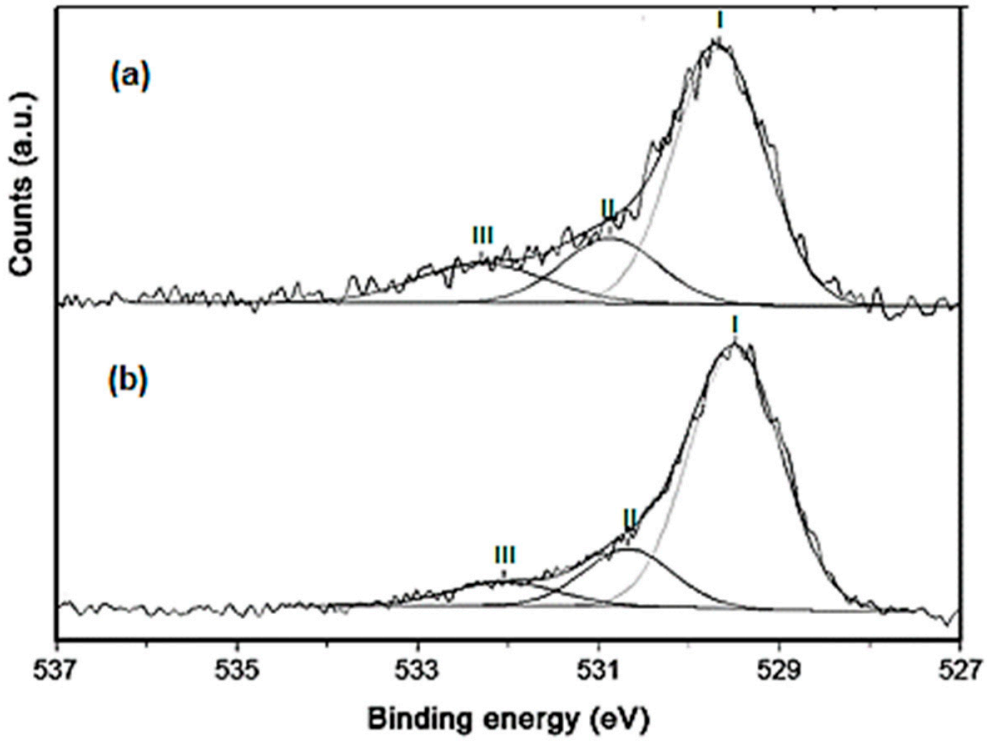

Figure 9. XPS spectra in the O1s region for the samples (**a**) 1077 and (**b**) AH-R.

(i) In gas phase, the acetone is fully mineralized, thus exchanging 16 electrons with the photocatalyst. This assumption is not relevant, as even with partial mineralization we could estimate j_{PC}.
(ii) The total real area of the photocatalyst is exposed to the reactive medium. Thus, the surface area (S_{BET}) and amount (m) of photocatalyst are relevant parameters when estimating j_{PC}.
(iii) The value of j_{PEC} (aqueous phase) should be renormalized with respect to the surface area of the electrode in order to compare its magnitude with j_{PC} (gas phase). This normalization implicitly assumes the electrolyte permeates all the nanostructured thin film electrodes studied.

Hence, the apparent current density in gas phase will be given by

$$j_{PC} = \frac{zFv}{S_{BET}m} \quad (2)$$

where z is the number of exchanged electrons (16 for full acetone mineralization); F is the Faraday constant (96,485 C·mol^{-1}), and v is the reaction rate (mol·s^{-1}) estimated from the slope of curves in Figure 8 in the time range from 0 to 40 min. In addition, the normalized open-circuit current density in aqueous phase with respect to the real surface are will be

$$j_{PEC} = j\left(\frac{S}{pS_{BET}m}\right) \quad (3)$$

where j is the open-circuit current density values taken from Figure 7, S is the geometric exposed area of the electrodes (1 cm^2), and p is the porosity of the film (taken as 0.50; this means only half of the total surface area is exposed to the electrolyte, as particles merge during electrode preparation and its real area is hence reduced). The amount of catalyst is estimated assuming all doctor bladed dispersion is deposited on the FTO substrates. In Figure 10, we gather all estimated current densities and their relationship.

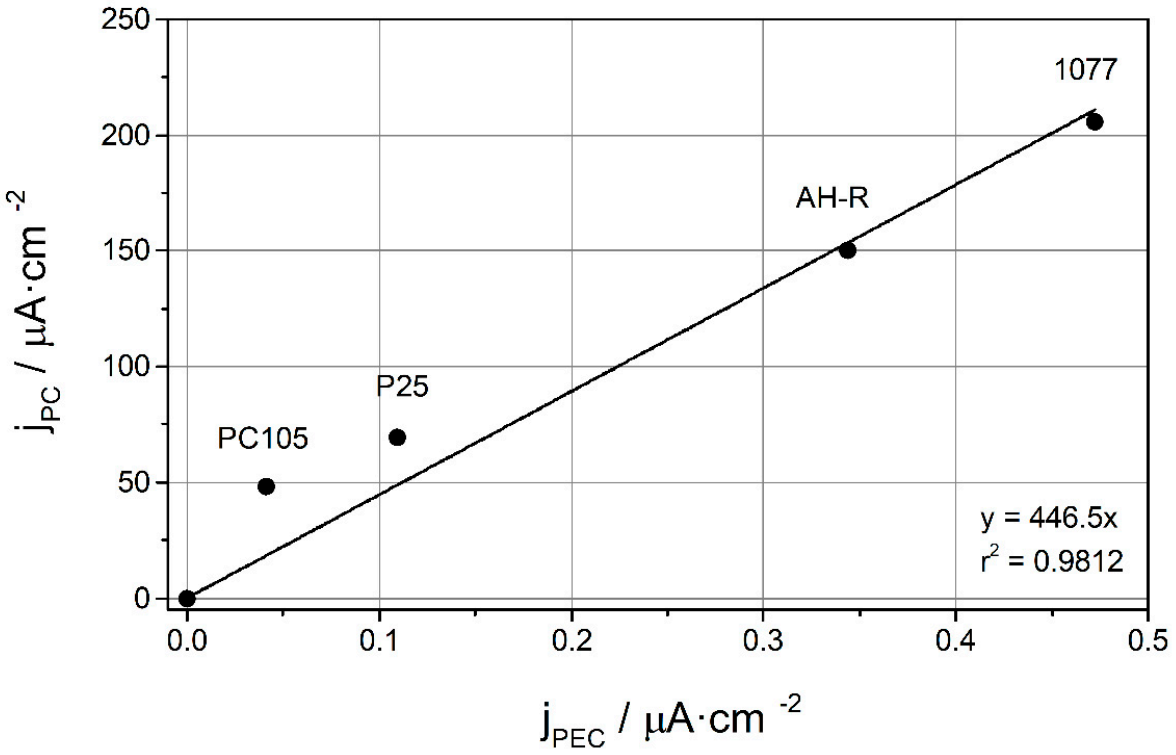

Figure 10. Linear correlation between the apparent open-circuit current density in the gas phase (j_{PC}) with the open-circuit current density in the aqueous phase (j_{PEC}) for the photocatalytic degradation of acetone. The values of S_{BET} and m per each photocatalyst were taken from the Experimental section. The (0,0) point was intentionally added to avoid any violation of the fundamental principles of photochemistry.

As observed, there is a reasonably good linear correlation between j_{PC} and j_{PEC}, which could be used to predict the behavior in one phase given the same in the other phase. It should be noted that the correlation is valid for this particular reaction and set of photocatalysts, and by no means can it be extended to any gas phase reaction. In any case, this correlation points out that the nature of the media (gas or liquid) where the photocatalytic degradation of acetone takes place is not significantly relevant; this could be explained in terms of the acetone interaction with the titania surface, that is governing the reaction mechanism [40,44]. Interestingly, the activity ordering of the photocatalysts seems to be reversed with respect to prior measurements, as sub-micro sized powders (1077 and AH-R) now apparently appear more active than the nanosized powders (PC105 and P25); however, we should note this is only stemming from the definition of current densities, as we have expressed them in terms of the surface area, thus catalysts with larger values, will yield lower apparent current densities. Interestingly, the linear relationship between (apparent) current densities could be expressed as

$$j_{PC} = \frac{zF}{p}\left(\frac{v/m}{j/m'}\right) j_{PEC} \quad (4)$$

where m' is the mass of the deposited photocatalyst in the electrodes. As observed, the relationship does not depend on the surface area of the photocatalyst; nonetheless, the equation scales with the mass-normalized ratio of the gas phase rate and the aqueous phase current density.

3. Experimental Section

3.1. Reagents and Chemicals

Acetone is a Fluka product at high purity grade. Four commercial titanium dioxide samples, two nanometric (AEROXIDE® TiO_2 P25 by Evonik Ind. and PC105 by Crystal-

Global) and two sub-micrometric (1077 by Kronos and AH-R by Hundsman) were chosen as photocatalysts and used without any pre-treatment or activation.

3.2. Materials Characterization

The surface area of all samples was determined by conventional N_2 adsorption (BET) at 77 K using a sorptometer instrument (Costech Mod. 1042). X-ray photoelectron spectra (XPS) were taken in an M-probe apparatus (Surface Science Instruments). The source was monochromatic Al Kα radiation (1486.6 eV). The energy scale was calibrated with reference to the $4f_{7/2}$ level of freshly evaporated gold sample at 84.00 $\pm$ 0.1 eV. The accuracy of the reported BE can be estimated to be $\pm$0.2 eV. The morphology of the catalysts was investigated by high resolution electron transmission microscopy (HR-TEM). TEM images were recorded using a JEOL 3010-UHR instrument (acceleration potential: 300 kV; LaB_6 filament), with samples dry dispersed on lacey carbon Cu grids. Absorption/transmission IR spectra have been obtained on a Perkin–Elmer FT-IR System 2000 spectrophotometer equipped with a Hg–Cd–Te cryo-detector in the 7200–580 cm^{-1} range at a 2 cm^{-1} resolution (number of scans ~20). For IR analysis, powder catalyst has been compressed in self-supporting discs (of about 10 $mg \cdot cm^{-2}$) and placed in a homemade quartz cell, equipped with KBr windows and connected to a conventional high-vacuum line. Spectra were recorded at room temperature (RT) both in air and after prolonged outgassing at RT.

3.3. Preparation of Electrodes

TiO_2 electrodes were prepared by spreading an aqueous slurry of commercial nano-sized TiO_2 over a freshly cleaned conductive glass (fluorine-doped tin oxide, FTO glass). In order to have the same thickness of active material on the FTO surface, the suspension was prepared by adding 0.25 or 0.5 g of TiO_2 powder, respectively, for nanoparticles and sub-microparticles of TiO_2, to a mixture of distilled H_2O (1.25 mL for nanopowders and 1.00 mL for sub-micropowders), 15 µL of acetylacetone (Aldrich), and 15 µL of Triton X100 (Aldrich). In general, 15 µL of this suspension was dropped to an FTO glass, and a thin film of TiO_2 was obtained using the doctor blade method. Afterwards, the films were annealed and sintered for 2 h at 450 °C in air. The average thickness (in µm) was measured by means of a Profilometer Instrument (KLA-Tencor Alpha Step D-100) in two different portions of the TiO_2 annealed film.

3.4. Photo-Electrochemical Measurements

The measurements were carried out using a computer-controlled potentiostat (Autolab PGSTAT 30), and a 1000 W Hg-Xe arc lamp (Newport) as an illumination source. The experiments were performed in acidic medium, by using a 0.1 M $HClO_4$ aqueous solution in a conventional three-electrode photo-electrochemical cell equipped with a quartz window. The counter and reference electrodes were a Pt wire and an Ag/AgCl/KCl (3M) electrode, respectively. All the potentials are quoted against this reference electrode. Before each measurement, the cell was cleaned with an acidic and concentrated $KMnO_4$ solution overnight, cleaned with a H_2O_2/H_2SO_4 (1:1 vol.) solution and then thoroughly rinsed with distilled water. Finally, the voltammetric cell was boiled in distilled water with a few drops of H_2SO_4. The working solution was bubbled with N_2 for 20 min prior to the electrochemical measurements and then a nitrogen flux was passed over the solution to avoid the oxygen entry. All cyclic voltammograms (CVs) were recorded between -0.7 and 0.8 V vs. Ag/AgCl at a scan rate of 20 $mV \cdot s^{-1}$. For studying the reduction process, the electrolyte solution was saturated with O_2 by bubbling the gas for 30 min. When the oxidation process was studied, CV measurements of the TiO_2 electrodes were recorded under UV-A illumination using several acetone concentrations (from 1 mM to 1 M) in the N_2-purged electrolyte solution.

3.5. Photocatalytic Set-Up

The photocatalytic degradation of acetone in air was conducted in a Pyrex glass cylindrical reactor with a diameter of 200 mm and an effective volume of 5 L. The amount of catalyst (in the form of powder deposited from a 2-propanol slurry on a flat glass disk) used in the tests was 0.05 g [45]. The gaseous mixture in the reactor was obtained by mixing hot chromatographic air, humidified at 40%, and a fixed amount of volatilized pollutant, in order to avoid condensation. The initial concentration of acetone in the reactor was 400 ppm. The photon source was a 500 W iron halogenide lamp (Jelosil, model HG 500) emitting in the 315–400 nm wavelength range (UV-A) at 30 $W \cdot m^{-2}$. Acetone tests lasted for 2 h. The actual concentration of pollutant adsorbed on TiO_2 in the reactor was determined directly by micro-GC sampling.

4. Conclusions

Photo-electrochemical and photocatalytic studies were conducted on nano- and submicrosized TiO_2 commercial samples, comparing them for the photodegradation of acetone, a typical indoor pollutant. It was found that a high concentration of pollutant inhibits photo-electrochemical degradation. Importantly, both smaller- and larger-sized TiO_2 nanosamples revealed that the optimal concentration for the oxidation of acetone was close to 10 mM. Nanometric samples were found to exhibit higher photocurrents than submicrosized ones. The potential photocatalytic activity of the samples was evaluated by comparing the j-E curves obtained in the presence of oxygen in the dark and in the presence of acetone (10 mM) under UV illumination. The best efficiency was obtained for nanometric P25, which generates an equivalent photocurrent under open circuit conditions higher (0.08 mA/cm^2) than in the other ones. Otherwise, both nano-sized PC105 and larger-sized AH-R have the similar values of photocurrent (0.03 mA/cm^2), resulting more active than the other larger-sized sample (1077). It is remarkable that a nanocrystalline and a microcrystalline sample display similar efficiency. This is a result of the existence of two separate factors: increased surface area (in smaller-sized samples) and the existence of an operating space charge layer (in larger-sized samples). Among the different TiO_2 samples, PC105 and P25 exhibit the best results in photocatalytic gaseous oxidation. On the contrary, 1077 has better photoefficiency than AH-R, as shown by the faster oxidation rate. This feature could be explained by the amount of photoactive "free" Ti-OH sites, which are probably responsible for photooxidation. In summary, it is important to highlight that larger-sized samples have different behaviors depending on the nature of the catalytic processes. In photo-electrochemical analysis, not only the degree of hydroxilation but also the morphology and the particle size play an important role while for the photocatalysis in gas phase, OH radicals have a fundamental role. In this sense, larger-sized TiO_2 samples could be valuable candidates for the photooxidation of VOC in gas phase. Finally, a direct correlation between gas phase and aqueous phase measurements has been attempted, showing that both correlate pretty well; this evinces the role of the media in this particular reaction and with this set of photocatalysts does not seem relevant.

Author Contributions: Data curation, C.L.B.; formal analysis, P.B., D.M.-S. and G.C.; funding acquisition, C.L.B.; investigation, D.M.-S. and R.G.; supervision, R.D.; validation, L.O. All authors have read and agreed to the published version of the manuscript.

Funding: This work has been developed in part in the context of project RTI2018–102061–B–I00 financed by FEDER/Ministerio de Ciencia e Innovación-Agencia Estatal de Investigación.

Conflicts of Interest: The authors declare no conflict of interest.

References

1. Schneider, J.; Matsuoka, M.; Takeuchi, M.; Zhang, J.; Horiuchi, Y.; Anpo, M.; Bahnemann, D.W. Understanding TiO_2 photocatalysis: Mechanisms and materials. *Chem. Rev.* **2014**, *114*, 9919–9986. [CrossRef] [PubMed]
2. Djellabi, R.; Ghorab, M.F.; Smara, A.; Bianchi, C.L.; Cerrato, G.; Zhao, X.; Yang, B. *Titania–Montmorillonite for the Photocatalytic Removal of Contaminants from Water: Adsorb & Shuttle Process., Green Materials for Wastewater Treatment*; Springer: Berlin/Heidelberg, Germany, 2020; pp. 291–319.
3. Fagan, R.; McCormack, D.E.; Dionysiou, D.D.; Pillai, S.C. A review of solar and visible light active TiO_2 photocatalysis for treating bacteria, cyanotoxins and contaminants of emerging concern. *Mater. Sci. Semicond. Process.* **2016**, *42*, 2–14. [CrossRef]
4. Kang, X.; Liu, S.; Dai, Z.; He, Y.; Song, X.; Tan, Z. Titanium dioxide: From engineering to applications. *Catalysts* **2019**, *9*, 191. [CrossRef]
5. Lowry, G.V.; Gregory, K.B.; Apte, S.C.; Lead, J.R. *Transformations of Nanomaterials in the Environment*; ACS Publications: Washington, DC, USA, 2012.
6. Nam, Y.; Lim, J.H.; Ko, K.C.; Lee, J.Y. Photocatalytic activity of TiO_2 nanoparticles: A theoretical aspect. *J. Mater. Chem. A* **2019**, *7*, 13833–13859. [CrossRef]
7. Hou, J.; Wang, L.; Wang, C.; Zhang, S.; Liu, H.; Li, S.; Wang, X. Toxicity and mechanisms of action of titanium dioxide nanoparticles in living organisms. *J. Environ. Sci.* **2019**, *75*, 40–53. [CrossRef] [PubMed]
8. Park, S.; Lee, S.; Kim, B.; Lee, S.; Lee, J.; Sim, S.; Gu, M.; Yi, J.; Lee, J. Toxic effects of titanium dioxide nanoparticles on microbial activity and metabolic flux. *Biotechnol. Bioprocess Eng.* **2012**, *17*, 276–282. [CrossRef]
9. Baranowska-Wójcik, E.; Szwajgier, D.; Oleszczuk, P.; Winiarska-Mieczan, A. Effects of titanium dioxide nanoparticles exposure on human health—A review. *Biol. Trace Elem. Res.* **2020**, *193*, 118–129. [CrossRef]
10. Oravisjärvi, K.; Pietikäinen, M.; Ruuskanen, J.; Rautio, A.; Voutilainen, A.; Keiski, R.L. Effects of physical activity on the deposition of traffic-related particles into the human lungs in silico. *Sci. Total Environ.* **2011**, *409*, 4511–4518. [CrossRef]
11. Ai, J.; Biazar, E.; Jafarpour, M.; Montazeri, M.; Majdi, A.; Aminifard, S.; Zafari, M.; Akbari, H.R.; Rad, H.G. Nanotoxicology and nanoparticle safety in biomedical designs. *Int. J. Nanomed.* **2011**, *6*, 1117.
12. Xiong, S.; George, S.; Ji, Z.; Lin, S.; Yu, H.; Damoiseaux, R.; France, B.; Ng, K.W.; Loo, S.C.J. Size of TiO_2 nanoparticles influences their phototoxicity: An in vitro investigation. *Arch. Toxicol.* **2013**, *87*, 99–109. [CrossRef]
13. Cai, K.; Hou, Y.; Hu, Y.; Zhao, L.; Luo, Z.; Shi, Y.; Lai, M.; Yang, W.; Liu, P. Correlation of the cytotoxicity of TiO_2 nanoparticles with different particle sizes on a sub-200-nm scale. *Small* **2011**, *7*, 3026–3031. [CrossRef]
14. Bianchi, C.; Gatto, S.; Pirola, C.; Naldoni, A.; Di Michele, A.; Cerrato, G.; Crocella, V.; Capucci, V. Photocatalytic degradation of acetone, acetaldehyde and toluene in gas-phase: Comparison between nano and micro-sized TiO_2. *Appl. Catal. B Environ.* **2014**, *146*, 123–130. [CrossRef]
15. Bianchi, C.L.; Sacchi, B.; Pirola, C.; DeMartin, F.; Cerrato, G.; Morandi, S.; Capucci, V. Aspirin and paracetamol removal using a commercial micro-sized TiO_2 catalyst in deionized and tap water. *Environ. Sci. Pollut. Res.* **2016**, *24*, 12646–12654. [CrossRef] [PubMed]
16. Bianchi, C.L.; Colombo, E.; Gatto, S.; Stucchi, M.; Cerrato, G.; Morandi, S.; Capucci, V. Photocatalytic degradation of dyes in water with micro-sized TiO_2 as powder or coated on porcelain-grès tiles. *J. Photochem. Photobiol. A Chem.* **2014**, *280*, 27–31. [CrossRef]
17. Djellabi, R.; Ghorab, M.F.; Sehili, T. Simultaneous removal of methylene blue and hexavalent chromium from water using TiO_2/Fe(III)/H_2O_2/sunlight. *Clean-Soil Air Water* **2017**, *45*, 1500379. [CrossRef]
18. Chen, S.; Thind, S.S.; Chen, A. Nanostructured materials for water splitting-state of the art and future needs: A mini-review. *Electrochem. Commun.* **2016**, *63*, 10–17. [CrossRef]
19. Ho-Kimura, S.; Moniz, S.J.A.; Handoko, A.D.; Tang, J. Enhanced photoelectrochemical water splitting by nanostructured $BiVO_4$–TiO_2 composite electrodes. *J. Mater. Chem. A* **2014**, *2*, 3948–3953. [CrossRef]
20. Jafari, T.; Moharreri, E.; Amin, A.S.; Miao, R.; Song, W.; Suib, S.L. Photocatalytic water splitting—The untamed dream: A review of recent advances. *Molecules* **2016**, *21*, 900. [CrossRef] [PubMed]
21. Szymanski, P.; El-Sayed, M.A. *Some Recent Developments in Photoelectrochemical Water Splitting Using Nanostructured TiO_2: A Short Review*; Marco Antonio Chaer Nascimento; Springer: Berlin/Heidelberg, Germany, 2014; pp. 7–18.
22. Mais, L.; Mascia, M.; Palmas, S.; Vacca, A. Photoelectrochemical oxidation of phenol with nanostructured TiO_2-PANI electrodes under solar light irradiation. *Sep. Purif. Technol.* **2019**, *208*, 153–159. [CrossRef]
23. Kondalkar, V.V.; Mali, S.S.; Mane, R.M.; Dandge, P.B.; Choudhury, S.; Hong, C.K.; Patil, P.S.; Patil, S.R.; Kim, J.H.; Bhosale, P.N. Photoelectrocatalysis of cefotaxime using nanostructured TiO_2 photoanode: Identification of the degradation products and determination of the toxicity level. *Ind. Eng. Chem. Res.* **2014**, *53*, 18152–18162. [CrossRef]
24. Tang, Y.; Ren, H.; Huang, J. Synthesis of porous TiO_2 nanowires and their photocatalytic properties. *Front. Optoelectron.* **2017**, *10*, 395–401. [CrossRef]
25. Zhang, J.; Djellabi, R.; Zhao, S.; Qiao, M.; Jiang, F.; Yan, M.; Zhao, X. Recovery of phosphorus and metallic nickel along with HCl production from electroless nickel plating effluents: The key role of three-compartment photoelectrocatalytic cell system. *J. Hazard. Mater.* **2020**, *394*, 122559. [CrossRef] [PubMed]
26. Zhang, J.; Zhao, X.; Wang, Y.; Djellabi, R. Recovery of Phosphorus from Hypophosphite-Laden Wastewater: A Single-Compartment Photoelectrocatalytic Cell System Integrating Oxidation and Precipitation. *Environ. Sci. Technol.* **2019**, *54*, 1204–1213. [CrossRef]

27. Monllor-Satoca, D.; Lana-Villarreal, T.; Gómez, R. Effect of surface fluorination on the electrochemical and photoelectrocatalytic properties of nanoporous titanium dioxide electrodes. *Langmuir* **2011**, *27*, 15312–15321. [CrossRef]
28. Hwang, Y.J.; Hahn, C.; Liu, B.; Yang, P. Photoelectrochemical properties of TiO_2 nanowire arrays: A study of the dependence on length and atomic layer deposition coating. *ACS Nano* **2012**, *6*, 5060–5069. [CrossRef]
29. Ochiai, T.; Fujishima, A. Photoelectrochemical properties of TiO_2 photocatalyst and its applications for environmental purification. *J. Photochem. Photobiol. C Photochem. Rev.* **2012**, *13*, 247–262. [CrossRef]
30. Acevedo-Peña, P.; González, I. Relation between morphology and photoelectrochemical performance of TiO_2 nanotubes arrays grown in ethylene glycol/water. *Procedia Chem.* **2014**, *12*, 34–40. [CrossRef]
31. Ennaceri, H.; Fischer, K.; Hanus, K.; Chemseddine, A.; Prager, A.; Griebel, J.; Kühnert, M.; Schulze, A.; Abel, B. Effect of Morphology on the Photoelectrochemical Activity of TiO_2 Self-Organized Nanotube Arrays. *Catalysts* **2020**, *10*, 279. [CrossRef]
32. Ibadurrohman, M.; Hellgardt, K. Morphological modification of TiO_2 thin films as highly efficient photoanodes for photoelectrochemical water splitting. *ACS Appl. Mater. Interfaces* **2015**, *7*, 9088–9097. [CrossRef]
33. Lana-Villarreal, T.; Mao, Y.; Wong, S.S.; Gómez, R. Photoelectrochemical behaviour of anatase nanoporous films: Effect of the nanoparticle organization. *Nanoscale* **2010**, *2*, 1690–1698. [CrossRef]
34. Bickley, R.I.; Gonzalez-Carreno, T.; Lees, J.S.; Palmisano, L.; Tilley, R.J. A structural investigation of titanium dioxide photocatalysts. *J. Solid State Chem.* **1991**, *92*, 178–190. [CrossRef]
35. Djellabi, R.; Yang, B.; Wang, Y.; Cui, X.; Zhao, X. Carbonaceous biomass-titania composites with Ti–O–C bonding bridge for efficient photocatalytic reduction of Cr(VI) under narrow visible light. *Chem. Eng. J.* **2019**, *366*, 172–180. [CrossRef]
36. Djellabi, R.; Yang, B.; Xiao, K.; Gong, Y.; Cao, D.; Sharif, H.M.A.; Zhao, X.; Zhu, C.; Zhang, J. Unravelling the mechanistic role of Ti–O–C bonding bridge at titania/lignocellulosic biomass interface for Cr(VI) photoreduction under visible light. *J. Colloid Interface Sci.* **2019**, *553*, 409–417. [CrossRef]
37. Berger, T.; Lana-Villarreal, T.; Monllor-Satoca, D.; Gómez, R. Thin films of rutile quantum-size nanowires as electrodes: Photoelectrochemical studies. *J. Phys. Chem. C* **2008**, *112*, 15920–15928. [CrossRef]
38. Jankulovska, M.; Barceló, I.; Lana-Villarreal, T.; Gómez, R. Improving the photoelectrochemical response of TiO_2 nanotubes upon decoration with quantum-sized anatase nanowires. *J. Phys. Chem. C* **2013**, *117*, 4024–4031. [CrossRef]
39. Lyon, L.A.; Hupp, J.T. Energetics of semiconductor electrode/solution interfaces: EQCM evidence for charge-compensating cation adsorption and intercalation during accumulation layer formation in the titanium dioxide/acetonitrile system. *J. Phys. Chem.* **1995**, *99*, 15718–15720. [CrossRef]
40. Berger, T.; Monllor-Satoca, D.; Jankulovska, M.; Lana-Villarreal, T.; Gómez, R. The electrochemistry of nanostructured titanium dioxide electrodes. *ChemPhysChem* **2012**, *13*, 2824–2875. [CrossRef]
41. Morand, R.; Lopez, C.; Koudelka-Hep, M.; Kędzierzawski, P.; Augustynski, J. Photoelectrochemical behavior in low-conductivity media of nanostructured TiO_2 films deposited on interdigitated microelectrode arrays. *J. Phys. Chem. B* **2002**, *106*, 7218–7224. [CrossRef]
42. Kesselman, J.M.; Shreve, G.A.; Hoffmann, M.R.; Lewis, N.S. Flux-matching conditions at TiO_2 photoelectrodes: Is interfacial electron transfer to O_2 rate-limiting in the TiO_2-catalyzed photochemical degradation of organics? *J. Phys. Chem.* **1994**, *98*, 13385–13395. [CrossRef]
43. Bullock, E.; Patthey, L.; Steinemann, S. Clean and hydroxylated rutile TiO_2(110) surfaces studied by X-ray photoelectron spectroscopy. *Surf. Sci.* **1996**, *352–354*, 504–510. [CrossRef]
44. Monllor-Satoca, D.; Díez-García, M.I.; Lana-Villarreal, T.; Gómez, R. Photoelectrocatalytic production of solar fuels with semiconductor oxides: Materials, activity and modeling. *Chem. Commun.* **2020**, *56*, 12272–12289. [CrossRef] [PubMed]
45. Bianchi, C.L.; Pirola, C.; Selli, E.; Biella, S. Photocatalytic NO_x abatement: The role of the material supporting the TiO_2 active layer. *J. Hazard. Mater.* **2012**, *211*, 203–207. [CrossRef] [PubMed]